

Dynamic compression of copper to over 450 GPa: A high-pressure standard

R. G. Kraus¹, J.-P. Davis², C. T. Seagle², D. E. Fratanduono¹, D. C. Swift¹, J. L. Brown², J. H. Eggert¹

¹*Lawrence Livermore National Laboratory, Livermore, CA, USA*

²*Sandia National Laboratories, Albuquerque, NM, USA*

Abstract

An absolute stress-density path for shocklessly compressed copper is obtained to over 450 GPa. A magnetic pressure drive is temporally tailored to generate shockless compression waves through over 2.5 mm thick copper samples. The free-surface velocity data is analyzed for Lagrangian sound velocity using the iterative Lagrangian analysis (ILA) technique, which relies upon the method of characteristics. We correct for the effects of strength and plastic work heating to determine an isentropic compression path. By assuming a Debye model for the heat capacity, we can further correct the isentrope to an isotherm. Our determination of the isentrope and isotherm of copper represents a highly accurate pressure standard for copper to over 450 GPa. (?/??? words)

Key words: DYNAMIC COMPRESSION EXPERIMENTS, MATERIAL STRENGTH, EQUATION OF STATE, PRESSURE STANDARD

1. Introduction

The high-pressure and low-temperature equation of state is critical to a number of natural science and engineering studies. For example, the equation of state of hydrogen is the dominant source of uncertainty in our understanding of the structure and composition of Jupiter's core [1], which has significant implications for our understanding of the formation of planets in our solar system. The abundance of extrasolar planets in the 1-10 Earth mass range is generating significant interest in the the high-pressure properties of planetary minerals due to their effect on the structure and thermal evolution of super Earths and correspondingly potential planetary habitability. Central to these low-temperature high-pressure studies is the existence of a standard method of determining the stress state being studied. Attempts to develop accurate isothermal absolute-pressure standards using Brillouin scattering and x-ray diffraction have been limited to below 60 GPa [2], and therefore at higher pressures shock Hugoniot data are often used to constrain the low temperature isotherm due to the exact nature of the Rankine-Hugoniot relations, [e.g. 3, 4]. However, these shock-wave reduced isotherms (SWRI) require significant corrections from the measured Hugoniot states as the shock pressure and shock heating increases. Furthermore, the models for the thermal pressure are oftentimes not constrained by experimental data but determined from theoretical calculations, inhibiting rigorous error propagation. With the advancement of single stage diamond anvil cells reaching pressures of 375 GPa[5] and the advent of two-stage diamond anvil cells capable of reaching pressures greater than 770 GPa[6, 7], there is a tremendous need for accurate pressure calibrants and rigorous error

26 analysis in the range accessible to this novel diamond anvil cell technology.

27 Copper is commonly used as a pressure standard within the high-pressure
28 community due to the availability of accurate shock wave data[3, 8, 9, 4].
29 However, as discussed in Ref. [4], the shock wave reduced isotherm for copper
30 is only valid to 200 GPa. The high-pressure behavior of copper is also critical
31 to the capabilities at the Sandia Z machine[10], where copper is used as an
32 electrode material in shockless compression experiments and as a flyer plate
33 for ultra-high velocity plate impact experiments [11]. Copper is also starting
34 to be utilized as an ablator material for shockless compression experiments
35 at the National Ignition Facility [e.g. 12], and validation or improvement
36 of the available equation of state models is critical to the design of future
37 experiments.

38 Shockless compression experiments have previously been used to deter-
39 mine the high-pressure and low-temperature response of aluminum [13], di-
40 amond [14, 12], and tantalum [15, 16]. In this work, we determine the stress-
41 density response of shocklessly compressed copper. Copper is an excellent
42 material to study by shockless compression experiments as it is expected to
43 have no high-pressure phase transitions and low shear strength.

44 Using the Z pulsed-power accelerator at Sandia National Laboratories[10],
45 magnetically driven uniaxial compression waves were generated in copper
46 samples that ranged in thickness from ~ 2.4 to 3 mm thick. The Z acceler-
47 ator produces a temporally shaped current pulse, of up to 20 MA and 1200
48 ns in duration, that flows along the inner surface of the copper electrodes,
49 generating a time-varying magnetic field. The interaction of the magnetic
50 field and the current flux produces a time varying force on the inner surface

51 of the copper electrodes, see schematic diagram in Figure 1. In the stripline
52 geometry, the samples on opposing sides of the short circuit loop undergo
53 identical loading conditions, making this an excellent platform for shockless
54 compression experiments.

55 **2. Experimental Method**

56 Two separate experiments, each with four sample pairs, were performed
57 on copper: experiments Z2689 and Z2791. The OFE-OK grade copper elec-
58 trodes were 99.998% pure with an average grain size of $80\ \mu\text{m}$ and a measured
59 HRF hardness of 43. The electrodes were $43.5\times 11\times 8\ \text{mm}$ and slightly ta-
60 pered at the base. Rectangular copper steps were diamond milled into the
61 solid electrode to generate samples of the desired thickness, between ~ 2.4
62 and $3\ \text{mm}$ thick and $9.0\times 7.7\ \text{mm}$ in lateral dimension. The thickness of each
63 copper sample was measured to an accuracy of $\sim 3\ \mu\text{m}$.

64 The multi-point quadrature velocity interferometer system for any re-
65 flector (VISAR) operated at $532\ \text{nm}$. Three separate VISAR sensitivities
66 were used on each sample, with fringe sensitivities that ranged from 257 to
67 $483\ \text{m s}^{-1}\ \text{fringe}^{-1}$. After correcting the absolute timing of each VISAR
68 channel for the etalon delay, individual free-surface velocities were averaged
69 to reduce random uncertainties in the timing of individual VISAR channels,
70 $\sim 0.2\ \text{ns}$, and the random phase uncertainty in the fringe count, $\sim 5\%$ of the
71 fringe sensitivity. Two-dimensional magneto-hydrodynamic (MHD) simula-
72 tions were performed to confirm that the $200\ \mu\text{m}$ bare optical VISAR fibers
73 were probing regions only undergoing uniaxial strain.

74 The averaged free-surface velocities from each sample pair for experiment

75 Z2689 and Z2791 are presented in Figures 2 and 3 respectively. One can see
76 that in shot Z2689, Figure 2, shockless compression data were obtained on
77 all of the pairs up to a free-surface velocity of $\sim 3.5 \text{ km s}^{-1}$. In shot Z2791,
78 Figure 3, the current pulse shape was modified in order to avoid a shock
79 forming in the middle of the pulse shape and shockless compression data
80 were obtained on two of the pairs, N01-S01 and N02-S02, up to the peak
81 free-surface velocity.

82 Due to the high electrical conductivity of copper, diffusion of the magnetic
83 field through the copper samples is relatively slow. However, on shot Z2791,
84 the pair N01-S01 shows that the peak velocity on N01 increases beyond the
85 peak velocity of S01. This deviation is caused by the reverberation of the
86 free-surface release wave with the magnetic diffusion front, which limits the
87 range of analyzable data [17].

88 **3. Results**

89 *3.1. Stress-Density Analysis During Shockless Compression Experiments*

90 In an ideal shockless compression experiment, one would measure the in-
91 material particle velocity as a function of time at multiple positions within
92 the compressed sample [18]. From the in-material particle velocity profiles,
93 the Lagrangian sound speed is determined by the difference in measurement
94 positions divided by the time it takes for a perturbation to travel from one
95 position to the next, where a perturbation could be defined as an incremental
96 increase in velocity. In this optimal shockless compression experiment, one
97 could determine the Lagrangian sound speed, C_L , as a nearly continuous
98 function of the in-material particle velocity, u_p , where $C_L = C_E \frac{\rho}{\rho_0}$ and C_E is

99 the Eulerian sound velocity.

100 While in-material particle velocity profiles can be measured on insulators
101 using techniques such as magnetic particle velocity gauges [19], for opaque
102 metals one cannot measure a true in-material particle velocity and velocity
103 profile measurements are limited to interfaces or free-surface velocity mea-
104 surements. The iterative Lagrangian analysis (ILA) method [20, 21] was
105 developed to correct for the effect of the free surface reflection, or map the
106 free-surface velocity profiles to in-material velocity profiles.

107 One way to consider the ILA method is that there is a unique solution
108 to the isentropic equation of state for the problem where samples of two
109 different thickness are shocklessly compressed by the same pressure boundary
110 condition and the free surface velocity profiles are the problem constraints.
111 The numerical techniques optimize over the equation of state and the pressure
112 boundary condition until a solution matching the free surface velocity profiles
113 is achieved. A more detailed description of the ILA method can be found in
114 Ref. [15].

115 Recent work has shown that small shocks have a weak effect on the de-
116 termination of the stress-density response using the ILA technique[22]; how-
117 ever, the data presented here are of sufficiently high accuracy to be sensitive
118 to the small systematic error induced by analyzing data with small shocks.
119 Therefore, only data without shocks are included in the analysis of the free-
120 surface velocity measurements; this includes all the pairs from shot Z2689 up
121 to 3.5 km s^{-1} . The data from Z2791 N01-S01 are included up to 8 km s^{-1}
122 and Z2791 N02-S02 up to 8.8 km s^{-1} . The sound speeds and residuals from
123 the weighted mean for each sample pair are presented as a function of free-

124 surface velocity in Figure 4.

125 The uncertainty in C_L is determined from the uncertainty in the slope of
 126 a fit to the Lagrangian thickness versus time for each particle velocity,

$$\left(\frac{\delta C_L}{C_L}\right)^2 = 2\left(\frac{\delta X}{X_2 - X_1}\right)^2 + 2\left(\frac{\delta t}{t_2 - t_1}\right)^2 + \left[\frac{\delta u_{p,1}}{(t_2 - t_1) du_{p,1}/dt}\right]^2 + \left[\frac{\delta u_{p,2}}{(t_2 - t_1) du_{p,2}/dt}\right]^2, \quad (1)$$

127 where $\delta X = 3 \mu\text{m}$ is the measured thickness uncertainty for each step height
 128 X_2 and X_1 , $\delta t = 0.12 \text{ ns}$ is the absolute timing uncertainty of the free-surface
 129 velocity profile, t_2 and t_1 are the in-material times where the steps reach the
 130 particle velocity of interest, $\delta u_{p,i} \approx 0.01 \text{ km s}^{-1}$ is the velocity uncertainty
 131 for profile i and $du_{p,i}/dt$ is the acceleration at the time of interest. Conse-
 132 quently, the uncertainty in C_L is $\sim 1\%$ for each sample pair. The weighted
 133 average Lagrangian sound velocity is determined as a function of free-surface
 134 velocity, weighted by $1/\delta C_L^2$. The uncertainty in this weighted average C_L is
 135 conservatively determined as the maximum of either the mean uncertainty
 136 in C_L , as determined by equation 1 or the standard deviation in C_L at each
 137 free-surface velocity.

138 The weighted average C_L can then be directly integrated to obtain the
 139 longitudinal stress, σ_x , and density, ρ , as a function of particle velocity, u_p ,

$$\sigma_x = \rho_0 \int_0^{u_p} C_L du_p \quad (2)$$

140 and

$$\rho = \rho_0 \left[1 - \left(\int_0^{u_p} \frac{du_p}{C_L} \right) \right]^{-1}. \quad (3)$$

141 The uncertainties are propagated through the integrals to obtain uncertain-
 142 ties in longitudinal stress and density,

$$\delta \sigma_x = \rho_0 \int_0^{u_p} \delta C_L du_p, \quad (4)$$

143 and

$$\delta\rho = \frac{\rho^2}{\rho_0} \int_0^{u_p} \frac{\delta C_L du_p}{C_L^2} \quad (5)$$

144 where the uncertainties are propagated linearly rather than in quadrature
145 because the errors appear to be correlated rather than random.

146 A more complete description of the ILA technique can be found in Ref.
147 [15]. Ref. [15] also describes some of the issues facing the assumption of
148 reversibility and isentropic flow inherent within the ILA technique, partic-
149 ularly for high-strength materials that exhibit significant time dependence.
150 As copper is expected to have relatively low strength and to stay within the
151 thermally activated regime over the stress range and strain rates considered
152 in this study [23], the effects of rate dependence or irreversible flow should be
153 negligible for copper. To test this assumption, we performed forward simula-
154 tions of the ramp compression experiments using the ARES hydrocode [24].
155 These simulations utilized the SESAME 3325 equation of state for copper [25]
156 and two different strength models: the standard time-independent Steinberg-
157 Guinan strength model [26] and the Preston-Tonks-Wallace (PTW) strength
158 model [23], which includes strain-rate dependence on the yield surface. We
159 find that the ILA of simulated data generated with the PTW strength model
160 disagrees with the simulated in-material stress density response by a small
161 systematic difference of 0.3% in stress over the entire density range of in-
162 terest, which is well below the experimental errors and thermo-mechanical
163 corrections described here. The ILA of simulated data generated with the
164 standard Steinberg-Guinan strength model is in nearly perfect agreement
165 with the true in-material stress density response over the entire range of inter-
166 est. Consequently, the ILA technique accurately determines the in-material

167 stress–density response and any systematic contributions due to the ILA
 168 technique itself are small and can be ignored for copper.

169 *3.2. Correcting Shockless Compression Data for Strength Effects*

170 Here we present a method for determining the principal isentrope and 298
 171 K isotherm from the stress–density states that are determined from a shock-
 172 less compression experiment. A correction is necessary because the stress-
 173 density path obtained by the ILA technique does not represent an isentrope
 174 due to strength and plastic work heating. For relatively low strength materi-
 175 als like copper, we find these corrections from the shockless compression data
 176 are small, $\sim 2 - 3\%$, but because of the high accuracy of the experimental
 177 measurements, $2 - 4\%$, these corrections are now significant.

178 At this point forward we are considering an analysis of the thermody-
 179 namic states at constant density, consequently, the uncertainty in density is
 180 accounted for in the uncertainty in the stress state,

$$\delta\sigma_x(\rho)^2 = \delta\sigma_x(u_p)^2 + \left(\frac{\partial\sigma_x}{\partial\rho} \delta\rho(u_p) \right)^2. \quad (6)$$

181 Under uniaxial strain conditions, the longitudinal stress, σ_x , deviates from
 182 the mean hydrostatic stress, P_{hyd} , by an amount s_x , referred to as the stress
 183 deviator,

$$\sigma_x = P_{hyd} + s_x. \quad (7)$$

184 The work done by the stress deviators against plastic deformation of the ma-
 185 terial increases the entropy and temperature of the system. This source of
 186 dissipation is referred to as plastic work heating. For uniaxial strain condi-
 187 tions, and assuming a von Mises yield criterion [27], the differential amount

188 of plastic work heating, dW_p can be determined by the following equation,
 189 derived in Ref. [28],

$$dW_p = \frac{1}{\rho_0} \frac{2}{3} Y [d\epsilon_x - (dY/2\mu)] \quad (8)$$

190 where Y is the yield strength, and μ is the shear modulus. For conditions of
 191 uniaxial strain, the natural strain, ϵ_x , is determined by the relative compres-
 192 sion of the system according to

$$\epsilon_x = \ln(\rho/\rho_0). \quad (9)$$

193 Assuming the material behaves quasi-harmonically, the plastic work heat-
 194 ing causes the mean hydrostatic pressure to deviate from an isentrope by

$$P_{hyd} - P_s = \gamma\rho \int_0^{\epsilon_x} \beta dW_p, \quad (10)$$

195 where γ is the Grüneisen parameter, P_s is the pressure on the principal isen-
 196 trope, and β is the Taylor-Quinney factor, which describes the fraction of
 197 plastic work that partitions into thermal energy of the system [29]. Ref. [29]
 198 found that for copper, $\beta=0.9$. More recently, Ref. [30] found that for poly-
 199 crystalline copper the Taylor-Quinney factor increases linearly with strain-
 200 rate from 0.5 to 0.7 over a strain rate of 3000 to 8000 s^{-1} . The experiments
 201 considered here are at significantly higher strain rate, $10^6 s^{-1}$, and a linear
 202 extrapolation of the results by Ref. [30] would suggest $\beta = 1$ at our high
 203 strain rates. In this work, we assume a β of 0.9; however, because the strong
 204 of copper is low, the amount of plastic work is also small and the choice of
 205 beta is relatively insensitive as to decrease β by 50% only changes the final
 206 pressure on the isentrope by 0.3%.

207 Here we have made the simplifying assumption that only the fraction of
 208 plastic work that goes into thermal energy contributes to the pressure of the
 209 system. The other $(1 - \beta)$ of plastic work contributes to the potential energy
 210 of the lattice by creating defects, which in keeping with the assumption of
 211 deriving Equation 8, is volume conserving.

212 3.2.1. Thermal Pressure Model

213 To determine the correction from the mean hydrostatic stress along the
 214 shockless compression path, P_{hyd} to the isentrope, P_s , we require a model for
 215 the Grüneisen parameter. The Grüneisen parameter is also useful for calcu-
 216 lating the temperature change along an isentrope. Fortunately, the shockless
 217 compression data obtained here can be combined with porous Hugoniot data
 218 [31, 32] and solid Hugoniot data [33, 34, 35] to constrain a Mie-Grüneisen
 219 equation of state for copper over the entire density range of interest. The
 220 Grüneisen parameter is determined at the density of each shock data point
 221 by the ratio of the difference in pressure to the difference in internal energy
 222 between the shock state, P_H and E_H , and the pressure and internal energy
 223 along an isentrope at the same density, P_S and E_S , respectively,

$$\gamma = \frac{(P_H - P_S)}{\rho(E_H - E_S)}, \quad (11)$$

224 where the internal energy on the Hugoniot is given by the Rankine-Hugoniot
 225 equations [36] and the internal energy along the isentrope is determined by
 226 integrating the first law of thermodynamics at constant entropy.

227 The data are fit to the Al'tshuler form of the density dependence of the
 228 Grüneisen parameter, which assumes the Grüneisen parameter is tempera-

229 ture independent,

$$\gamma = \gamma_{\infty} + (\gamma_0 - \gamma_{\infty}) \left(\frac{\rho_0}{\rho} \right)^{\eta}, \quad (12)$$

230 where γ_{∞} is the infinite compression limit, η describes the density depen-
231 dence, and γ_0 is the ambient pressure value, which we have fixed at the
232 standard temperature and pressure value of 2.0(0.1) [37]. In Figure 5, we
233 present the Grüneisen parameters obtained using Equation 11 for a range of
234 initially porous and solid density Hugoniot data on copper. Also presented in
235 Figure 5 is our weighted nonlinear least squares fit to Equation 12, where we
236 find $\gamma_{inf} = 1.41$ and $\eta = 13.6$. As mentioned earlier, here we have made the
237 assumption that the Grüneisen parameter is temperature independent. We
238 find that this is a valid assumption based upon the agreement between the
239 results of this technique and that of a local technique relating the sound speed
240 along the Hugoniot to the slope of the Hugoniot, where Ref. [38] measured
241 a γ of 1.55(15) at a density range of $\sim 14\text{--}15 \text{ g cm}^{-3}$ on the Hugoniot.

242 The standard deviation in the residuals and the average absolute residual
243 between the experimental Grüneisen parameter and the best fit model are
244 0.68 and 0.38, respectively, which we believe to be overestimates of the uncer-
245 tainty in the model as these metrics are dominated by a few data points with
246 large scatter at low compressions. However, for the purposes of uncertainty
247 propagation, we assume a $\sim 25\%$ uncertainty in the Grüneisen parameter,
248 which propagates to a 0.2% uncertainty in the pressure on the isentrope.
249 Unlike for shock-wave reduced isotherms, where the stress at high pressures
250 becomes extremely sensitive to the thermal pressure model, here we find the
251 pressure along the isentrope to be insensitive to the thermal model because
252 of the relatively small amount of heating in the shockless compression exper-

253 iment.

254 3.2.2. High Pressure Strength

255 The high-pressure yield strength of copper has been measured on the
256 shock Hugoniot by Ref. [39, 40] and the data are presented in Figure 6. The
257 high-pressure yield strength of copper has also been calculated using molec-
258 ular dynamics simulations by Ref. [41], which is in excellent agreement with
259 the experimental data. We use a scaled Steinberg-Guinan model to fit the
260 experimental yield strength of copper [26], where we scale the ambient pres-
261 sure yield strength parameter, Y_0 and find the best fit to the yield strength
262 data for $1.82Y_0$. In this case, the yield strength measurements on the copper
263 Hugoniot achieve a similar strain-rate to the shockless compression experi-
264 ments. Consequently, we feel it is adequate to use a strain rate independent
265 strength model, calibrated by gas gun data, to correct for the yield strength
266 in the shockless compression experiments.

267 In order to correct for the yield strength over the entire range of pres-
268 sures accessed by the shockless compression experiments, a significant ex-
269 trapolation of the scaled Steinberg-Guinan is required. To account for this
270 extrapolation in the correction at high pressures and at low temperatures
271 along the shockless compression path, we assume a 50% uncertainty to the
272 yield strength at high pressures. As copper is not expected to undergo a
273 phase transition, and the experimental data and theoretical predictions are
274 well represented by this empirical strength model, it is likely that we are
275 overestimating the uncertainty in the yield strength. However, even such a
276 large estimate in the uncertainty of the yield strength at high pressure only
277 corresponds to an $\sim 1\%$ uncertainty in the pressure on the isentrope. For

278 comparison, the magnitude of the individual corrections from the shockless
 279 compression data to the 298 K isotherm are presented in Figure 7.

280 3.2.3. Hydrostatic Hugoniot States

281 Although it is not often discussed in the literature, Hugoniot measure-
 282 ments should not be compared directly to equation of state models. One
 283 must correct Hugoniot data, at least within the solid phases, for the devia-
 284 toric stress and the thermal pressure generated due to plastic work heating.
 285 The plastic work heating along the Hugoniot can be calculated based upon
 286 the waste heat generated along the Rayleigh line by the longitudinal devia-
 287 toric stress, s_x [42],

$$W_{p,Hug} = s_x \left(\frac{1}{\rho_0} - \frac{1}{\rho} \right). \quad (13)$$

288 The hydrostatic Hugoniot for a material is then given by

$$P_{Hug} = \sigma_{x,Hug} - s_x - \gamma\rho\beta W_{p,Hug}, \quad (14)$$

289 where $\sigma_{x,Hug}$ is the longitudinal stress at the Hugoniot state. For copper,
 290 this correction is equivalent to reducing the shock wave velocity in the solid
 291 by $\sim 0.025 \text{ km s}^{-1}$ or $\sim 0.5\%$.

292 In order to correct all the porous Hugoniot and solid Hugoniot for strength
 293 effects, we must first determine the critical shock pressures for incipient melt-
 294 ing of copper along the porous and solid density Hugoniots. We fit a Simon
 295 equation to the high-pressure melt curve of Ref. [43],

$$T_{melt} = T_{Ref} \left(\frac{P - P_{Ref}}{a} + 1 \right)^{1/c} \quad (15)$$

296 and find $T_{ref}=1351 \text{ K}$, $a=16.304 \text{ GPa}$, and $c=1.8331$. To calculate the shock
 297 temperatures along the principal and porous Hugoniots, we use our data

298 along the isentrope as a reference curve and we assume copper behaves as a
299 quasi-harmonic Debye solid [44], with $\theta_0=343.5$ K. We find that the principal
300 Hugoniot intersects the high-pressure melt curve at 224 GPa, which is in good
301 agreement with the measured critical shock pressure for incipient melting of
302 232 GPa [38]. This agreement is surprisingly good, given that we did not
303 apply any anharmonic or electronic contributions to the heat capacity. We
304 then assume that copper loses all strength for shock temperatures above the
305 melt curve. These corrected hydrostatic Hugoniot points are used in the
306 calculation of the Grüneisen parameters and the stress along the principal
307 isentrope.

308 *3.2.4. Summary of the Method for Reducing Shockless Compression Data to* 309 *an Isentrope*

310 At this point, all aspects of correcting the shockless compression data to
311 the principal isentrope have been described in Sections 3.2.1, 3.2.2, and 3.2.3.
312 However, the procedure is slightly complicated as some of the terms in the
313 correction require information about the isentrope. Therefore, we use an iter-
314 ative procedure to self-consistently solve for the pressure along the isentrope.
315 This iterative procedure is as follows:

- 316 1. Determine a model for the density dependence of the Grüneisen param-
317 eter using available Hugoniot data and assuming our shockless compres-
318 sion data represent an isentrope, see Section 3.2.1.
- 319 2. Fit the strength data on the Hugoniot of copper to the Steinberg-
320 Guinan model by scaling Y_0 . Model the strength along the ramp
321 compression path based upon the fit to Hugoniot strength data and

- 322 corrected for the lower temperature along the shockless compression
 323 path, see Section 3.2.2.
- 324 3. Calculate the plastic work heating and the thermal pressure from plas-
 325 tic work heating along the shockless compression path using Equa-
 326 tions 8 and 10.
 - 327 4. Determine the pressure along the isentrope by subtracting the devia-
 328 toric stress and the thermal pressure from the shockless compression
 329 path, Equations 7 and 10.
 - 330 5. Calculate the plastic work heating at each Hugoniot point below the
 331 melt curve using Equation 13.
 - 332 6. Determine the pressure along the hydrostatic Hugoniot states by sub-
 333 tracting the deviatoric stress and thermal pressure, Equation 14.
 - 334 7. Repeat steps 1-6 with the revised model for the isentrope, hydrostatic
 335 Hugoniot points, and Grüneisen parameter.

336 The corrections for the strength, and thermal pressure due to plastic work
 337 heating are only a few percent, Figure 7, and consequently, this procedure
 338 converges in only two iterations.

339 To determine the pressure along the 298 K isotherm, one must subtract
 340 the thermal pressure from the isentrope at the elevated temperature along
 341 the isentrope, T_s ,

$$P_{298} = P_s - \gamma\rho[E_{th.}(T_s) - E_{th.}(298)], \quad (16)$$

342 where $E_{th.}$ is the thermal energy at density ρ determined from the Debye
 343 integral [44] and the temperature along the isentrope is determined from
 344 integrating the thermodynamic derivative, $\gamma = \frac{\partial \ln T_s}{\partial \ln \rho}$.

345 As in Ref. [4], a higher order Vinet equation of state was then fit to the
 346 isentrope, isotherm, and shockless compression path. The fitting form is

$$P(X) = 3K_0 \left[(1 - X^{1/3}) / X^{2/3} \right] \exp \left[\eta (1 - X^{1/3}) + \beta (1 - X^{1/3})^2 + \psi (1 - X^{1/3})^3 \right] \quad (17)$$

347 where $X = \rho_0/\rho$, and the best fit parameters K_0 , η , β , and ψ are described
 348 in Table 1. The maximum deviation between the fits and the data is 3 GPa
 349 at the peak stress state and significantly better at lower pressures; however,
 350 the fits are to be used as interpolating functions and are not necessarily valid
 351 in extrapolation.

352 In Figures 8 and 9, we present the 298 K isotherm determined from this
 353 study. One can see that the isotherm agrees within 2% of that of Ref. [9]
 354 up to 65 GPa, where the thermal pressure on the Hugoniot is starting to no
 355 longer be negligible. Beyond 65 GPa, our 298 K isotherm is slightly stiffer
 356 than the results of Ref. [9] and [4], by about 6 GPa at 150 GPa, which is
 357 just outside our 1- σ uncertainty of 5 GPa. It is interesting to see that careful
 358 fitting of high-accuracy but low-pressure thermodynamic data on copper by
 359 Holzapfel [45], with a smooth extrapolation to the Fermi gas limit yields a
 360 nearly perfect agreement with the isotherm determined in this work.

361 3.3. Ruby R1-Line Calibration

362 The most common pressure standard within the high pressure diamond
 363 anvil cell community is the ruby R-line luminescence [46, 47]. Utilizing the
 364 quasi-hydrostatic compression data on copper and ruby presented in Ref.
 365 [9], we are able to re-calibrate the high-pressure ruby scale using our 298 K
 366 isotherm for copper. Here we assume the standard power law expansion for

367 the hydrostatic pressure as a function of the shift in the Ruby R1 line [3],

$$P = \frac{A}{B} \left[\left(\frac{\lambda}{\lambda_0} \right)^B - 1 \right] \quad (18)$$

368 where we find the best fit parameters $A=1915.1$ GPa and $B=10.603$.

369 The main source of uncertainty in this ruby calibration is the uncertainty
370 in the copper isotherm, $\sim 3\%$ in stress at 150 GPa, see Table 1 for upper and
371 lower bounds. Ref. [48] notes the possibility of a 1-2% systematic uncertainty
372 in the stress due to potential non-hydrostatic stresses in the medium used in
373 the diamond anvil cell (DAC) experiments of Ref. [9], which also contributes
374 to the uncertainty in our ruby calibration. Other sources of uncertainty,
375 such as the determination of the R1 line position and the density of copper
376 as determined by XRD in the DAC, are small [9].

377 In Figure 11, we present a comparison of our ruby calibration with the
378 ruby calibrations of Mao et al. [46], Aleksandrov et al. [49], Holzappel et
379 al. [50], Dewaele et al. [9], and Chijioke et al. [48]. The comparisons are
380 plotted to 200 GPa to show how each of the fits extrapolates, however, the
381 data upon which these fits are based only extend to pressures as high as 150
382 GPa [9]. One can see that the ruby calibration fits from Refs. [48, 51, 45]
383 are well within the error bars of this work and that the ruby calibration from
384 Refs. [49, 9] are $1-\sigma$ away from this revised fit.

385 4. Discussion

386 The dominant contribution to the uncertainty in the isotherm of copper
387 is the random experimental errors associated with the uncertainty in the
388 step thicknesses, the uncertainty in the relative timing of the free-surface

389 velocity profiles, and the uncertainty in the measured free-surface velocity
390 of the shockless compression experiments. These separate uncertainties all
391 contribute relatively equally to the total random experimental uncertainty in
392 stress at a given density, ranging from $\sim 2\%$ at 50 GPa to $\sim 4.5\%$ at 450 GPa.
393 The other major sources of uncertainty are the high-pressure strength of
394 copper, $\sim 1\%$, the Taylor-Quinney factor, $\sim 0.3\%$, and the Grüneisen model,
395 $\sim 0.2\%$.

396 These uncertainty contributions are not, however, unique to shockless
397 compression experiments. For shock experiments below the melt tempera-
398 ture, there will be a deviatoric stress contribution to the longitudinal stress
399 and also thermal pressure generated from plastic work heating. The amount
400 of plastic work that goes into thermal energy, and therefore thermal pressure,
401 is still parameterized by the Taylor-Quinney factor. For shock temperatures
402 above the melt curve, there is significant uncertainty in the latent heat of
403 melting at constant volume.

404 Where this thermo-mechanical reduction technique for obtaining isotherms
405 from shockless compression data becomes much more accurate than shock
406 wave reduced isotherms is at pressures well above the bulk modulus, where
407 several tens of percent corrections are required from the pressure at the Hugo-
408 niot state to the pressure on the isotherm. As an example, at a density of
409 17 g cm^{-3} , the pressure on the 298 K isotherm is ~ 450 GPa, whereas the
410 pressure on the principal Hugoniot is ~ 780 GPa, consequently, a thermal
411 pressure correction of 330 GPa is required for the shock wave data. For an
412 assumed 10-25% uncertainty in the Grüneisen parameter and a 5% uncer-
413 tainty in the Hugoniot pressure [34], the total uncertainty in the SWRI would

414 range between 50 and 100 GPa, or two to four times the uncertainty in the
415 isotherm obtained from reducing shockless compression data. A compari-
416 son of the required corrections for the SWRI-technique and the technique
417 described here are presented in Figure 10. The specific cross-over pressure
418 where isotherms reduced from shockless compression experiments becomes
419 more accurate than SWRI’s depends most sensitively on the uncertainty in
420 the Grüneisen parameter. If one assumes a 10% uncertainty in the Grüneisen
421 parameter, the SWRI will be more accurate up to 250 GPa on the isotherm;
422 however, if one assumes a 25% uncertainty in the Grüneisen parameter then
423 the SWRI will be more accurate only up to ~ 70 GPa.

424 Furthermore, as two-stage diamond anvil cells become more prevalent in
425 the static high-pressure community, the materials used as pressure standards
426 will reach densities where the SWRI technique is no longer viable. Shock-
427 less or multi-shock techniques will be the only means of obtaining accurate
428 pressure calibrations in the terapascal regime.

429 **5. Conclusions**

430 We have obtained shockless compression data on copper to over 450 GPa
431 using a magnetically applied pressure drive at the Sandia Z Machine. The
432 free-surface velocity data were analyzed using the ILA technique to obtain
433 the Lagrangian sound speed as a function of particle velocity. The Lagrangian
434 sound speed was then integrated to determine an absolute stress-density path.
435 The available data on the high-pressure strength of copper was combined to
436 constrain a modified Steinberg-Guinan strength model. A Mie-Grüneisen
437 Debye thermal model was then iteratively fit to the shockless compression

438 data and the available principal and porous Hugoniot data. The shockless
439 compression stress-density data were corrected for the deviatoric stress and
440 thermal pressure due to plastic work heating to generate a nearly absolute
441 principal isentrope. The principal isentrope was then corrected using our best
442 fit Mie-Grüneisen Debye model to obtain the room temperature isotherm
443 of copper to 450 GPa with an uncertainty of less than 5% at the highest
444 pressures obtained. A high precision fit to the shockless compression data,
445 the isentrope, the isotherm, and a new ruby calibration are presented for
446 immediate use for the purposes of pressure calibration within a diamond
447 anvil cell.

448 **6. Acknowledgments**

449 The authors wish to acknowledge the support of the large inter-disciplinary
450 team it takes to design, fabricate, and execute experiments on the Z machine.
451 We also thank Marius Millot, Tom Arsenlis, and Rip Collins for helpful com-
452 ments on the manuscript. This work was performed under the auspices of
453 the U.S. Department of Energy by Lawrence Livermore National Labora-
454 tory under Contract DE-AC52-07NA27344. Sandia National Laboratories
455 is a multi-program laboratory managed and operated by Sandia Corpora-
456 tion, a wholly owned subsidiary of Lockheed Martin Corporation, for the
457 U.S. Department of Energy's National Nuclear Security Administration un-
458 der contract DE-AC04-94AL85000.

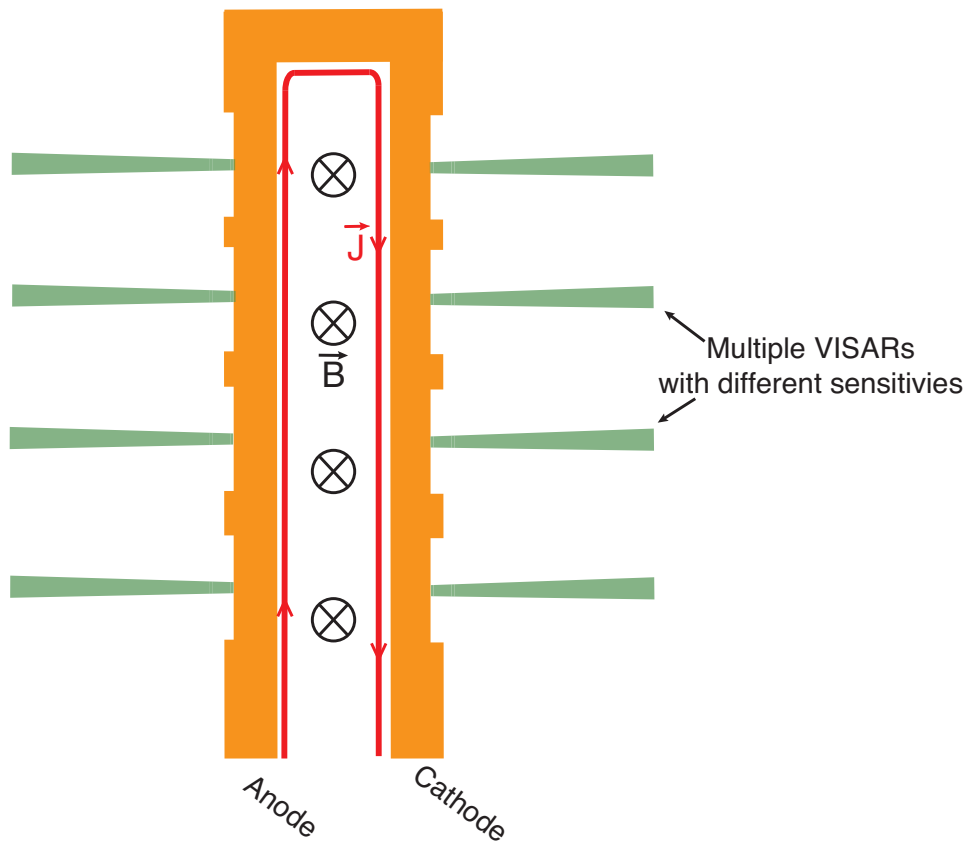


Figure 1: Schematic stripline geometry used for the shockless compression experiment on copper. The current density (J) flows on the inner surface of the anode to the cathode, creating a magnetic field vector (B), which interacts with the current density and accelerates the anode and cathode away from each other. VISAR probes measure the free surface velocity of the copper anode and cathode and are shown in green.

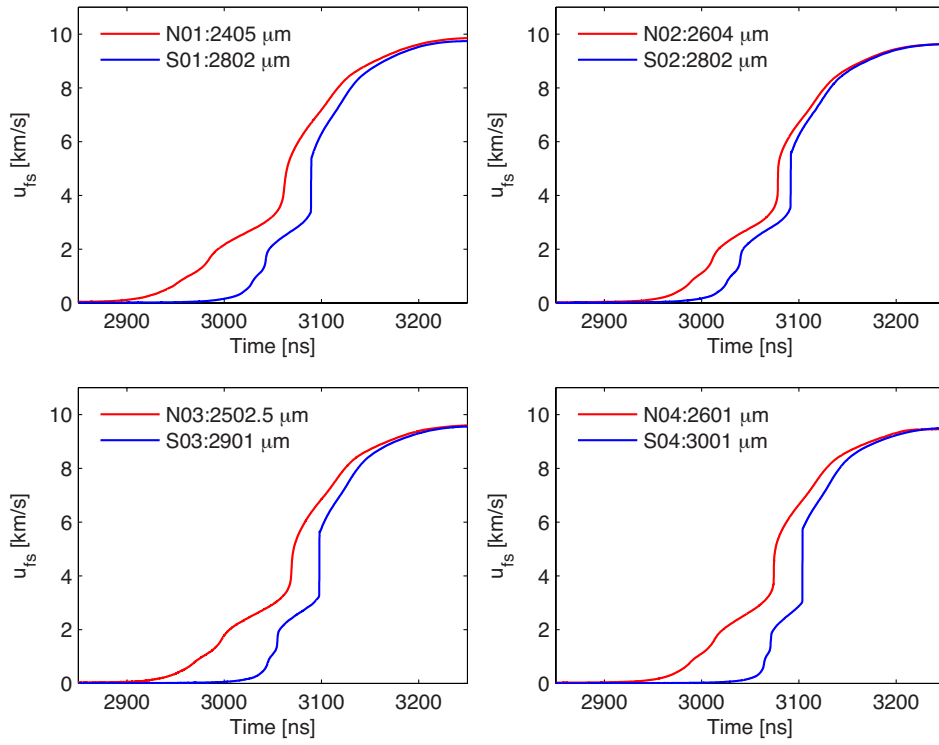


Figure 2: Average free-surface velocity profiles for each of the four pairs of samples on shot Z2689. Shown within each subplot are the thickness measurements for both of the samples.

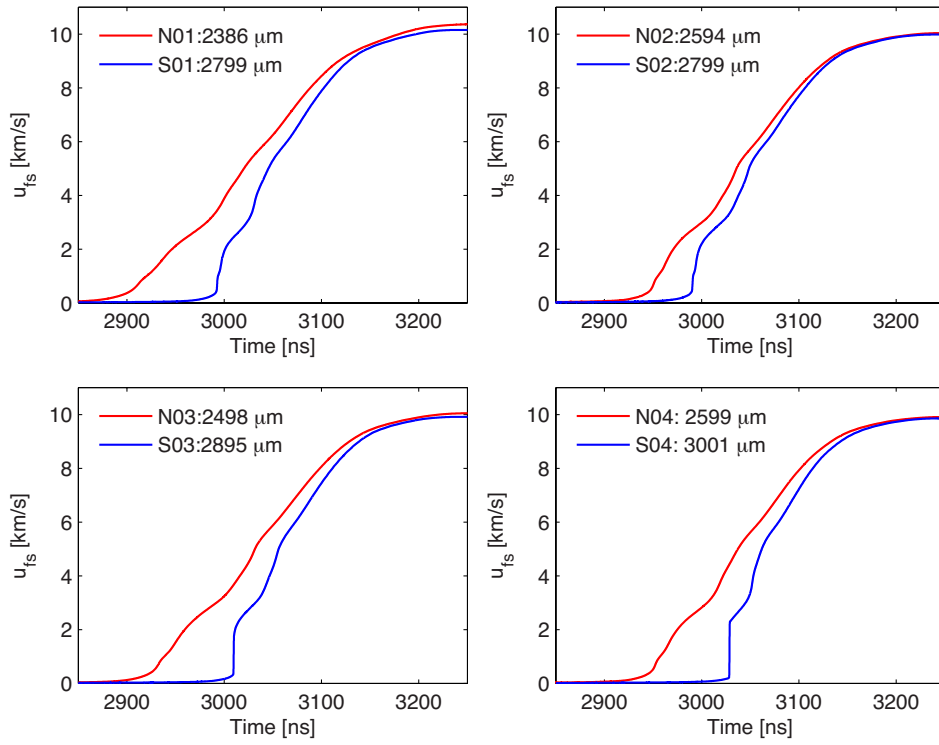


Figure 3: Average free-surface velocity profiles for each of the four pairs of samples on shot Z2791. Shown within each subplot are the thickness measurements for both of the samples.

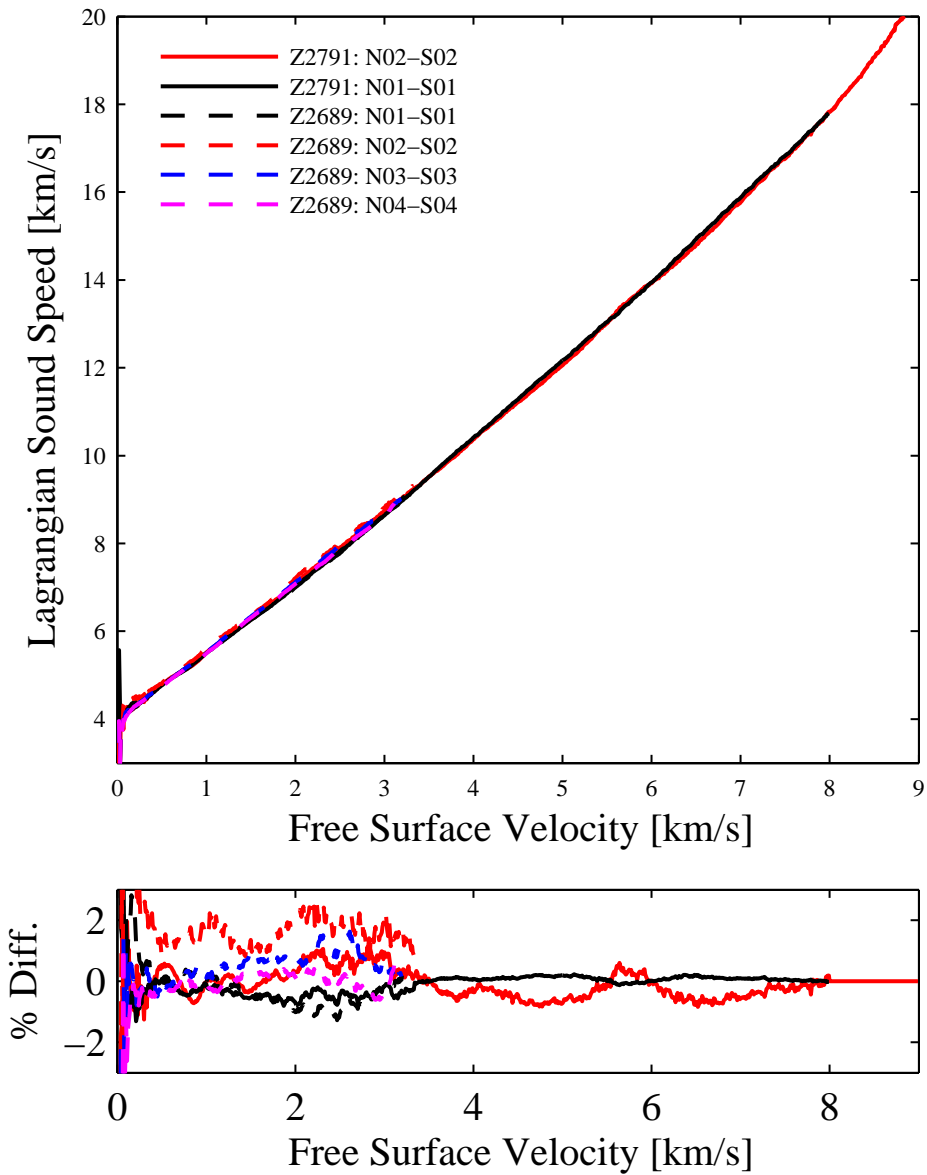


Figure 4: Measured Lagrangian sound velocity as a function of the free-surface velocity for two pairs on shot Z2791 (solid lines) and 4 pairs on shot Z2689 (dashed lines). Below are plotted the residuals for each of the sound velocity measurements relative to the weighted average sound velocity of all the traces.

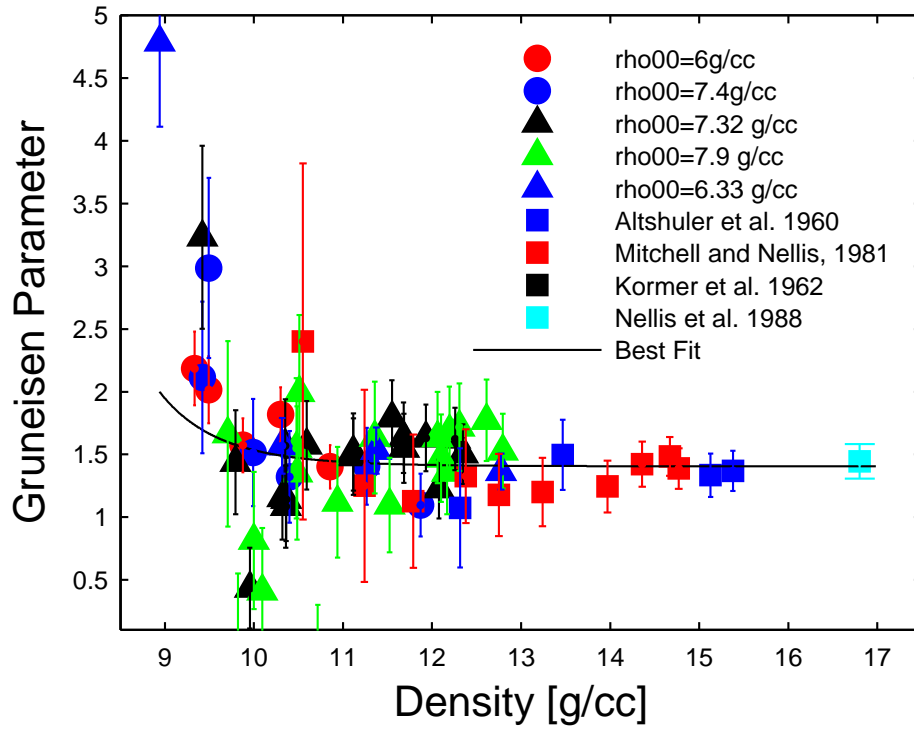


Figure 5: Grüneisen parameter determined from comparison of principal and porous Hugoniot data with measured isentrope. Also included is our best fit.

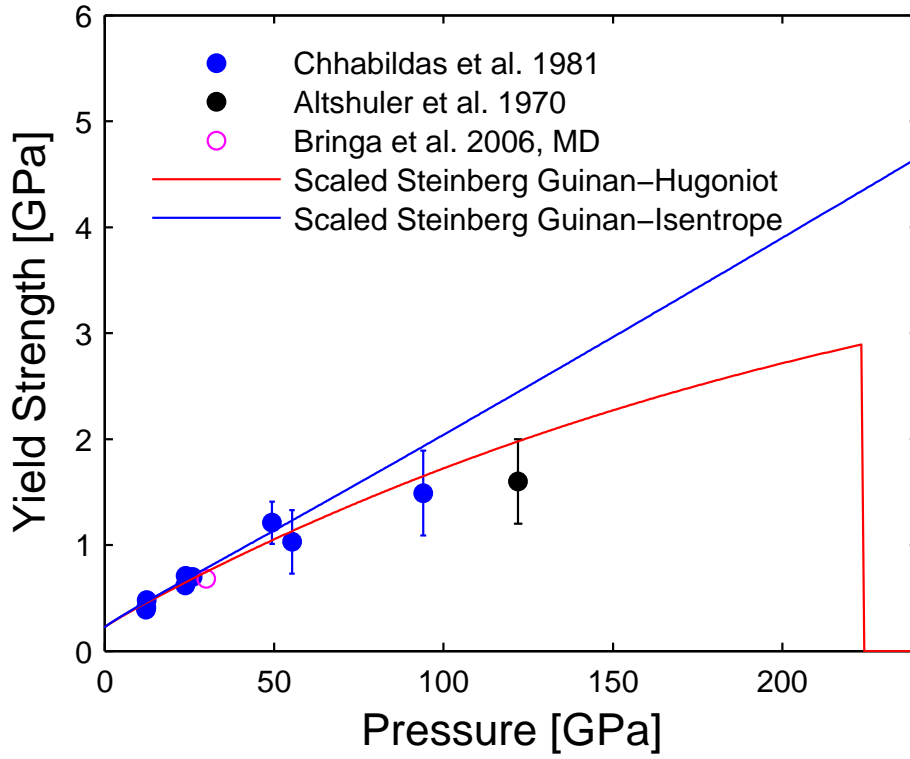


Figure 6: High-pressure yield strength data determined along the principal Hugoniot. Also presented is a scaled fit to the Steinberg-Guinan strength model along the Hugoniot (red) and isentrope (blue), where the strength along the Hugoniot drops to zero at 224 GPa due to shock melting.

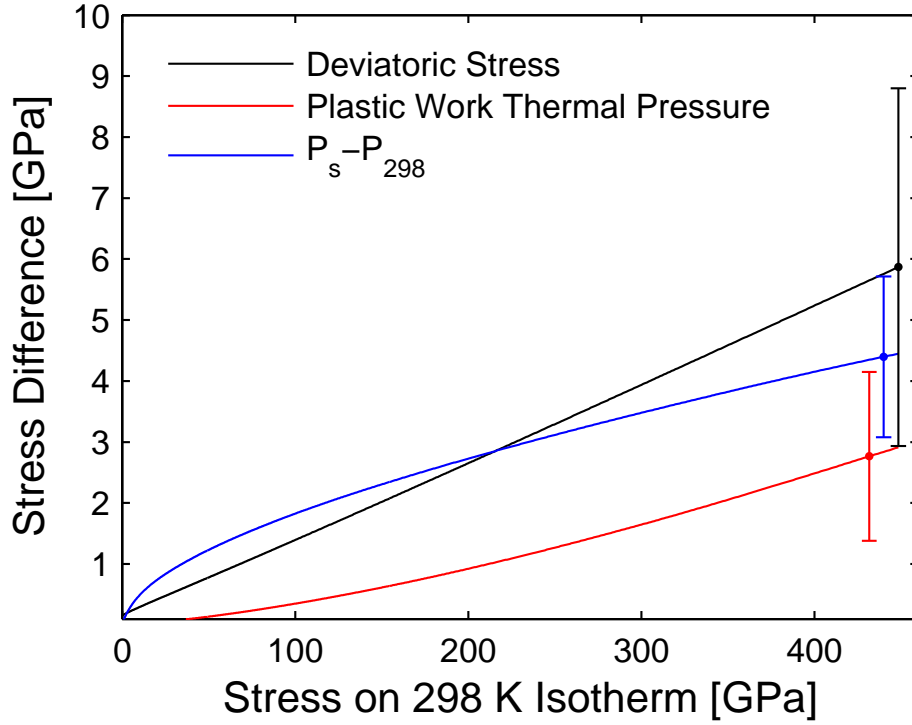


Figure 7: Required corrections and associated uncertainties for reducing shockless compression data to the 298 K isotherm of copper. Plotted are the corrections for the deviatoric stress (black), thermal pressure due to plastic work heating (red), and thermal pressure correction from the principal isentrope to the 298 K isotherm (blue solid line).

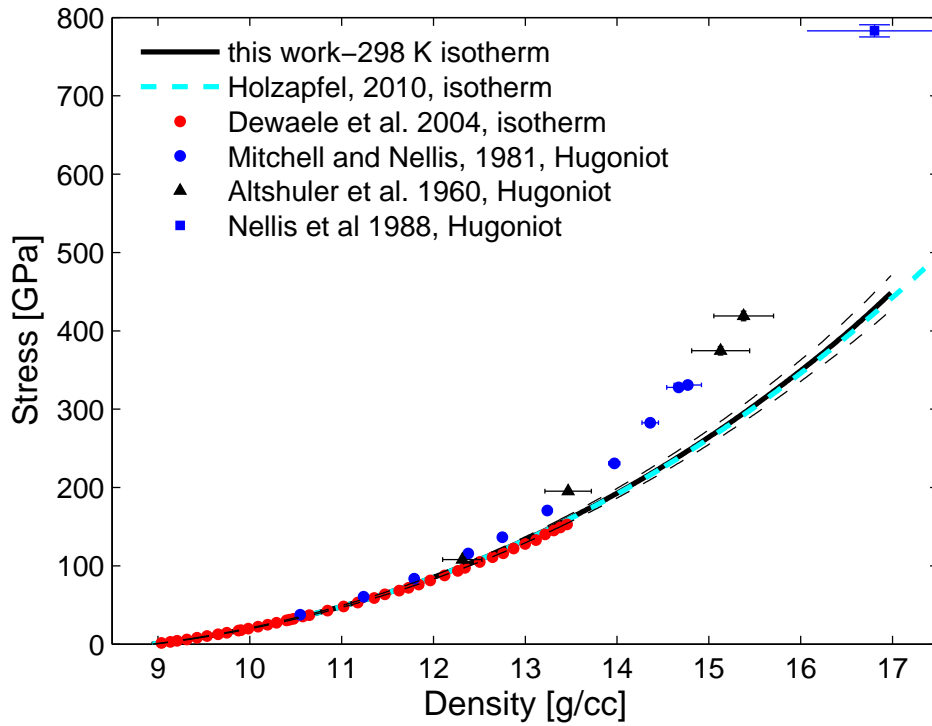


Figure 8: Equation of state data for copper on the principal Hugoniot and the 298 K isotherm. Shown are Hugoniot data from Mitchell and Nellis [34], Altshuler et al. [33], and Nellis et al. [35]; and isotherms from Dewaele et al. [9], Holzapfel [45], and this work.

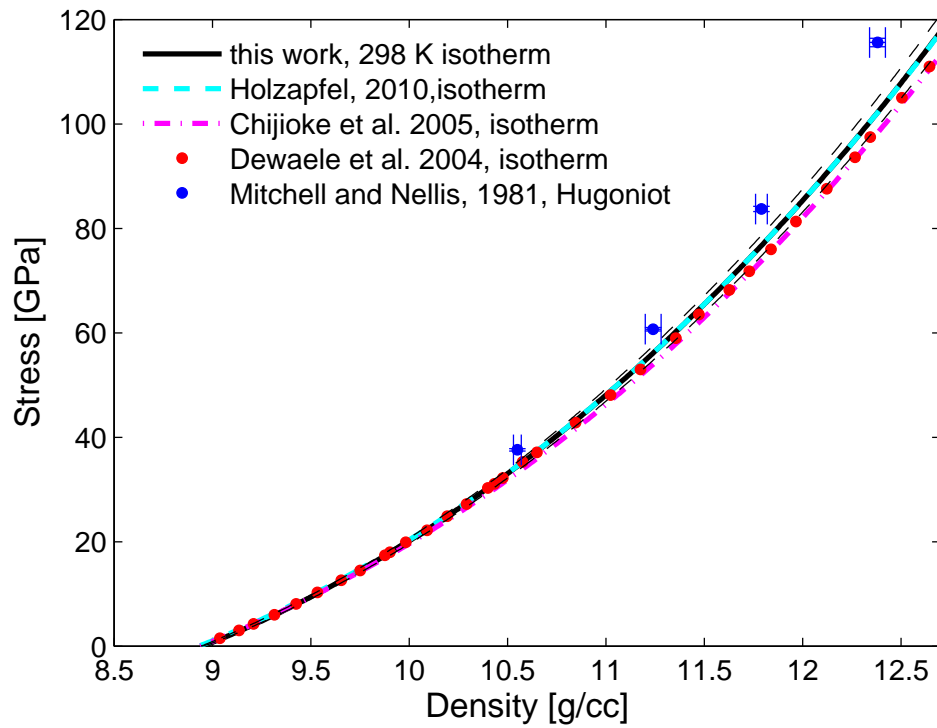


Figure 9: Equation of state data for copper up to 120 GPa. Shown are Hugoniot data from Mitchell and Nellis [34], and isotherms from Dewaele et al. [9], Chijioke et al. [4], Holzapfel [45] and this work.

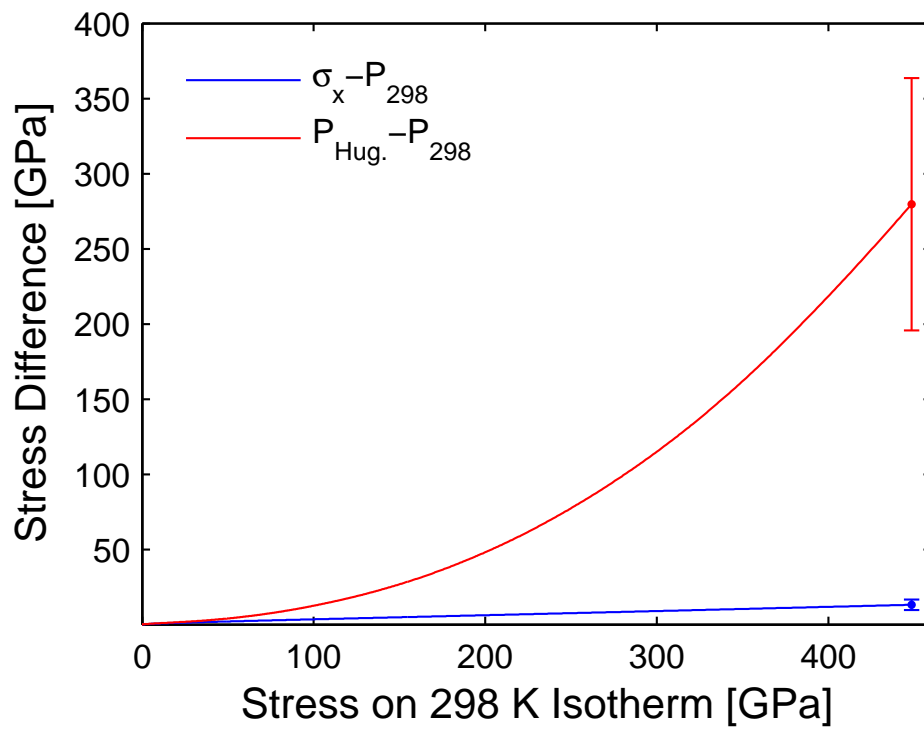


Figure 10: Sum total of the required corrections and associated uncertainties for reducing shock compression data (red) and shockless compression data (blue) to the 298 K isotherm of copper.

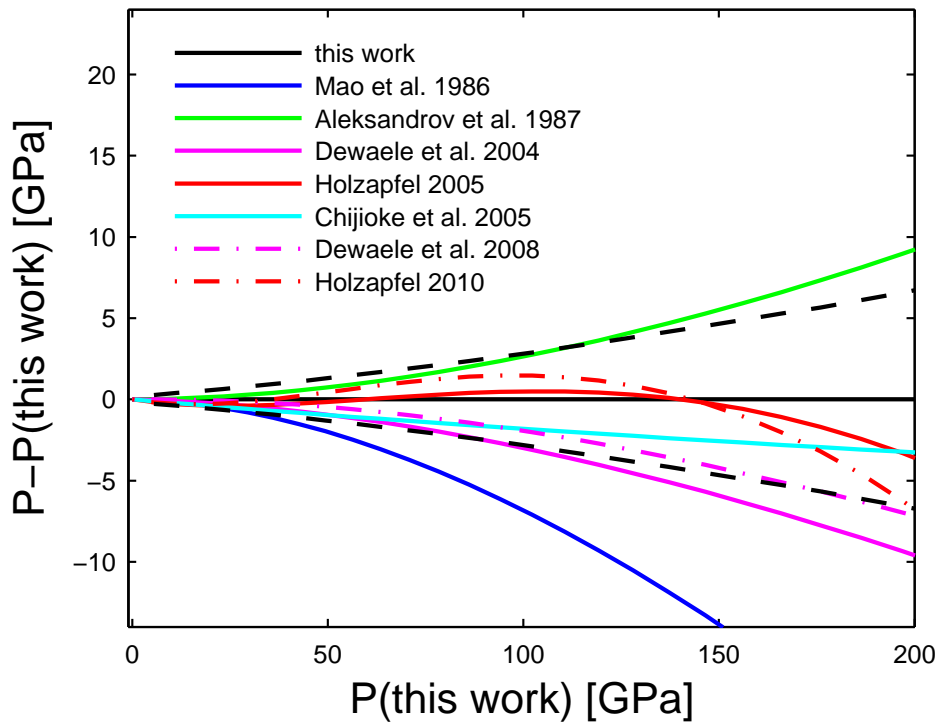


Figure 11: Comparison of fits to the pressure dependence of the ruby R1 line by Mao et al. [46], Aleksandrov et al. [49], Dewaele et al. [9], Holzzapfel [51], Chijioke et al. [48], Dewaele et al. [52], Holzzapfel [45], and this work. Also shown as black dashed lines are the 1- σ uncertainty bounds on the ruby R1 line calibration of this work. Above 150 GPa, these fits are no longer constrained by data and are presented as extrapolations for comparison purposes.

Table 1: Best fit parameters for the third order Vinet fit, Eqn. 17, to the shockless compression data, the principal isentrope, and the 298 K isotherm starting at an initial density of 8.939 g cm^{-3} . For the purposes of error propagation, also shown are fits to the upper and lower $1\text{-}\sigma$ uncertainty bounds on each fit.

Thermodynamic Path	K_0 [GPa]	η	β	ψ
Shockless Expt.	143.39	6.109	2.1348	4.567
Shockless: Upper	151.52	4.9902	12.858	-23.575
Shockless: Lower	135.4	7.2838	-9.1176	34.055
Principal Isentrope	136.35	7.1173	-7.1245	30.58
Isentrope: Upper	144.01	6.0987	2.5918	5.2783
Isentrope: Lower	128.8	8.1918	-17.365	57.209
298 K Isotherm	127.61	8.151	-14.452	49.034
Isotherm: Upper	134.69	7.1621	-5.0546	24.726
Isotherm: Lower	120.62	9.1941	-24.357	74.617

459 **References**

- 460 [1] J. J. Lissauer, D. J. Stevenson, Formation of giant planets, in:
461 B. Reipurth, D. Jewitt, K. Keil (Eds.), *Protostars and Planets V*, Uni-
462 versity of Arizona Press, Phoenix, AZ, 2006, pp. 591–606.
- 463 [2] D. M. Trots, A. Kurnosov, T. B. Ballaran, S. Tkachev, K. Zhuravlev,
464 V. Prakapenka, M. Berkowski, D. J. Frost, The Sm:YAG primary fluo-
465 rescence pressure scale, *Journal of Geophysical Research: Solid Earth* 118
466 (2013) 5805–5813.
- 467 [3] H. K. Mao, P. M. Bell, J. W. Shaner, D. J. Steinberg, Specific volume
468 measurements of Cu, Mo, Pd, and Ag and calibration of the ruby R1
469 fluorescence pressure gauge from 0.06 to 1 Mbar, *J. Appl. Phys.* 49 (1978)
470 3276.
- 471 [4] A. D. Chijioke, W. J. Nellis, I. F. Silvera, High-pressure equations of state
472 of Al, Cu, Ta, and W, *J. Appl. Phys.* 98 (2005) 073526.
- 473 [5] S. Tatenno, K. Hirose, Y. Oshishi, Y. Tatsumi, The structure of iron in
474 Earth’s inner core, *SCIENCE* 330 (2010) 359–361.
- 475 [6] L. Dubrovinsky, N. Dubrovinskaia, V. B. Prakapenka, A. M. Abakumov,
476 Implementation of micro-ball nano diamond anvils for high-pressure stud-
477 ies above 6 Mbar, *Nature Communications* 3 (2012) 1163.
- 478 [7] L. Dubrovinsky, N. Dubrovinskaia, E. Bykova, M. Bykov, V. B.
479 Prakapenka, C. Prescher, K. Glazyrin, H. P. Lierman, M. Hanfland,
480 M. Ekholm, Q. Feng, L. V. Pourovskii, M. I. Katsnelson, J. M. Wills,

- 481 I. A. Abrikosov, The most incompressible metal osmium at static pres-
482 sures above 750 gigapascals, *Nature* 525 (2015) 226.
- 483 [8] Y. Wang, R. Ahuja, B. Johansson, Reduction of shock-wave data with
484 mean-field potential approach, *J. Appl. Phys.* 92 (2002) 6616.
- 485 [9] A. Dewaele, P. Loubeyre, M. Mezouar, Equations of state of six metals
486 above 94 GPa, *Phys. Rev. B.* 70 (2004) 094112.
- 487 [10] Savage, M.E. *et al.*, An overview of pulse compression and power flow
488 in the upgraded Z pulsed power driver, in: 2007 IEEE Pulsed Power Con-
489 ference, Vol. 1-4, 2007, p. 979.
- 490 [11] R. W. Lemke, M. D. Knudson, J.-P. Davis, Magnetically driven hyper-
491 velocity launch capability at the Sandia Z accelerator, *International Jour-
492 nal of Impact Engineering* 38 (2011) 480–485, DOI:10.1063/1.2084316.
- 493 [12] R. F. Smith, J. H. Eggert, R. Jeanloz, T. S. Duffy, D. G. Braun, J. R.
494 Patterson, R. E. Rudd, J. Biener, A. E. Lazicki, A. V. Hamza, J. Wang,
495 T. Braun, L. X. Benedict, P. M. Celliers, G. W. Collins, Ramp compression
496 of diamond to five terapascals, *Nature* 511 (2014) 330–333.
- 497 [13] J.-P. Davis, Experimental measurement of the principal isentrope for
498 aluminum 6061-T6 to 240 GPa, *J. Appl. Phys.* 99 (2006) 103512.
- 499 [14] D. K. Bradley, J. H. Eggert, R. F. Smith, S. T. Prisbrey, D. G. Hicks,
500 D. G. Braun, J. Biener, A. V. Hamza, R. E. Rudd, G. W. Collins, Diamond
501 at 800 GPa, *Physical Review Letters* 102 (2009) 075503.

- 502 [15] J.-P. Davis, J. L. Brown, M. D. Knudson, R. W. Lemke, Analysis of
503 shockless dynamic compression data on solids to multi-megabar pressures:
504 Application to tantalum, *J. Appl. Phys.* 116 (2014) 204503.
- 505 [16] J. H. Eggert, R. F. Smith, D. C. Swift, R. E. Rudd, D. E. Fratantuono,
506 D. G. Braun, J. A. Hawreliak, J. M. McNaney, G. W. Collins,
507 Ramp compression of tantalum to 330 GPa, *High Pressure Research* DOI:
508 10.1080/08957959.2015.1071361.
- 509 [17] J.-P. Davis, C. Deeney, M. D. Knudson, R. W. Lemke, T. D. Pointon,
510 D. E. Bliss, Magnetically driven isentropic compression to multimegabar
511 pressures using shaped current pulses on the Z accelerator, *Physics of
512 Plasmas* 12 (2005) 056310.
- 513 [18] J. B. Aidun, Y. M. Gupta, Analysis of lagrangian gauge measurements
514 of simple and nonsimple plane-waves, *Journal of Applied Physics* 69 (10)
515 (1991) 6998–7014.
- 516 [19] S. Sheffield, R. Gustavsen, R. Alcon, In-situ magnetic gauging technique
517 used at LANL-method and shock information obtained, in: M. Furnish,
518 L. Chhabildas, R. Hixson (Eds.), *Shock Compression of Condensed Matter
519 - 2000*, American Institute of Physics, Melville, NY, 2006, pp. 1207–1210.
- 520 [20] J. R. Maw, A characteristics code for analysis of isentropic compression
521 experiments, in: M. Furnish, Y. Gupta, J. Forbes (Eds.), *Shock Compression
522 of Condensed Matter - 2003*, Vol. 706, American Institute of Physics,
523 Melville, NY, 2004, pp. 1217–1220.

- 524 [21] S. D. Rothman, J. Maw, Characteristics analysis of isentropic compres-
525 sion experiments, *J. Phys. IV France* 134 (2006) 745–750.
- 526 [22] D. E. Fratanduono, R. F. Smith, D. G. Braun, J. R. Patterson, R. G.
527 Kraus, T. S. Perry, A. Arsenlis, G. W. Collins, J. H. Eggert, The effect
528 of nearly steady shock waves in ramp compression experiments, *J. Appl.*
529 *Phys.* 117 (2015) 245903.
- 530 [23] D. L. Preston, D. L. Tonks, D. C. Wallace, Model of plastic deformation
531 for extreme loading conditions, *J. Appl. Phys.* 93 (2003) 211–220,
532 DOI:10.1063/1.1524706.
- 533 [24] G. Bazan, ASCI code calculations of supernova hydrodynamic instabil-
534 ities, in: B. A. Remington (Ed.), *Proceedings from the 2nd International*
535 *Workshop on Laboratory Astrophysics with Intense Lasers*, Livermore,
536 CA, 1998, UCRL-ID-131978.
- 537 [25] J. H. Carpenter, Private Communication.
- 538 [26] D. J. Steinberg, S. G. Cochran, M. W. Guinan, A constitutive model for
539 metals applicable at high-strain rate, *J. Appl. Phys.* 51 (1980) 1498–1504.
- 540 [27] R. von Mises, *Mechanik der festen korper im plastisch deformablen zu-*
541 *stand*, *Nachr. Ges. Wiss. Gottingen* 1 (1913) 582.
- 542 [28] G.-R. Fowles, Shock wave compression of hardened and annealed 2024
543 aluminum, *J. Appl. Phys* 32 (1961) 1475.
- 544 [29] G. I. Taylor, H. Quinney, The latent energy remaining in a metal after
545 cold working, *Proceedings of the Royal Society of London* 143 (1934) 307.

- 546 [30] D. Rittel, A. A. Kidane, M. Alkhader, A. Venkert, P. Landau,
547 G. Ravichandran, On the dynamically stored energy of cold work in pure
548 single crystal and polycrystalline copper, *Acta Materialia* 60 (2012) 3719–
549 3728.
- 550 [31] R.-R. Boade, Compression of porous copper by shock waves, *J. Appl.*
551 *Phys.* 39 (1968) 5693.
- 552 [32] S. P. Marsh, *LASL Shock Hugoniot Data*, University of California Press,
553 Berkeley, California, 1980.
- 554 [33] L. Al'tshuler, S. B. Kormer, A. A. Bakanova, R. F. Trunin, Equation
555 of state for aluminum, copper, and lead in the high pressure region, *Sov.*
556 *Phys. JETP* 11 (1960) 573–579.
- 557 [34] A. C. Mitchell, W. J. Nellis, Shock compression of aluminum, copper,
558 and tantalum, *J. Appl. Phys.* 52 (1981) 3363.
- 559 [35] W. J. Nellis, J. A. Moriarty, A. C. Mitchell, M. Ross, R. G. Dandrea,
560 N. W. Ashcroft, N. C. Holmes, G. R. Gathers, Metals physics at ultrahigh
561 pressures: aluminum, copper, and lead as prototypes, *Phys. Rev. Lett.* 60
562 (1988) 1414–1417.
- 563 [36] Y. B. Zel'dovich, Y. P. Raizer, *Physics of Shock Waves and High-*
564 *Temperature Hydrodynamic Phenomena*, Dover Publications, Mineola,
565 New York, 1966.
- 566 [37] W. B. Holzapfel, M. Hartwig, W. Sievers, Equations of state for Cu, Ag,
567 and Au for wide ranges in temperature and pressure up to 500 GPa and
568 above, *J. Phys. Chem. Ref. Data* 30 (2001) 515–529.

- 569 [38] D. Hayes, R. S. Hixson, R. G. McQueen, High pressure elastic properties,
570 solid-liquid phase boundary and liquid equation of state from release wave
571 measurements in shock-loaded copper, in: M. Furnish, L. C. Chhabildas,
572 R. S. Hixson (Eds.), *Shock Compression of Condensed Matter - 1999*,
573 American Institute of Physics, Melville, NY, 2000, p. 483.
- 574 [39] L. D. Chhabildas, J. R. Asay, Time-resolved wave profile measurements
575 in copper to megabar pressures, in: T. Johansson, C. M. Backman, L. Teg-
576 ner (Eds.), *Proceedings of Eighth AIRAPT and 19th EHPRG*, 1981, pp.
577 183–189.
- 578 [40] L. Al'tshuler, S. B. Kormer, A. A. Bakanova, R. F. Trunin, Strength and
579 elasticity of iron and copper at high shock-wave compression pressures,
580 *Zhurnal Prikladnoi Mekhaniki i Tekhnicheskoi Fiziki* 6 (1971) 159–166.
- 581 [41] E. M. Bringa, K. Rosolankova, R. E. Rudd, B. A. Remington, J. S.
582 Wark, M. Duchaineau, D. H. Kalantar, J. Hawreliak, J. Belak, Shock
583 deformation of face-centred-cubic metals on sub nanosecond timescales,
584 *Nature Materials* 5 (2006) 805–809.
- 585 [42] D. C. Swift, A. Seifert, D. B. Holtkamp, V. W. Yuan, D. Bowman, D. A.
586 Clark, Explanation of anomalous shock temperatures in shock-loaded Mo
587 samples measured using neutron resonance spectroscopy, *Phys. Rev. B* 77
588 (2008) 092102.
- 589 [43] Y. N. Wu, L. P. Wang, Y. S. Huang, D. M. Wang, Melting of copper
590 under high pressures by molecular dynamics simulation, *Chemical Physics*
591 *Letters* 515 (2011) 217–220.

- 592 [44] C. Kittel, H. Kroemer, Thermal Physics, W. H. Freeman and Company,
593 New York, 1980.
- 594 [45] W. B. Holzapfel, Equations of state for Cu, Ag, and Au and problems
595 with shock wave reduced isotherms, High Pressure Research 30 (2010)
596 372–394.
- 597 [46] H. K. Mao, J. Xu, P. M. Bell, Calibration of the ruby pressure gauge
598 to 800 mbar under quasi-hydrostatic conditions, Journal of Geophysical
599 Research 91 (1986) 4673–4676.
- 600 [47] K. Syassen, Ruby under pressure, High Pressure Research 28 (2008)
601 75–126.
- 602 [48] A. D. Chijioke, W. J. Nellis, A. Soldatov, I. F. Silvera, The ruby pressure
603 standard to 150 GPa, J. Appl. Phys. 98 (2005) 114905.
- 604 [49] I. V. Aleksandrova, A. F. Goncharov, A. N. Zisman, S. M. Stishov,
605 Diamond at high pressures: Raman scattering of light, equation of state,
606 and high-pressure scale, Sov. Phys. JETP 66 (1987) 384.
- 607 [50] W. B. Holzapfel, Refinement of the ruby luminescence pressure scale, J.
608 Appl. Phys. 93 (2003) 114905.
- 609 [51] W. B. Holzapfel, Progress in the realization of a practical pressure scale
610 for the range 1-300 GPa, High Pressure Research 25 (2005) 87–96.
- 611 [52] A. Dewaele, M. Torrent, P. Loubeyre, M. Mezouar, Compression curves
612 of transition metals in the Mbar range: Experiments and projector
613 augmented-wave calculations, Phys. Rev. B. 78 (2008) 104102.